



# CHORUS

This is the accepted manuscript made available via CHORUS. The article has been published as:

## Stability and Band-Gap Tuning of the Chalcogenide Perovskite BaZrS<sub>3</sub> in Raman and Optical Investigations at High Pressures

Nelson Gross, Yi-Yang Sun, Samanthe Perera, Haolei Hui, Xiucheng Wei, Shengbai Zhang, Hao Zeng, and B. A. Weinstein

Phys. Rev. Applied **8**, 044014 — Published 25 October 2017

DOI: [10.1103/PhysRevApplied.8.044014](https://doi.org/10.1103/PhysRevApplied.8.044014)

# Stability and band gap tuning of the chalcogenide perovskite BaZrS<sub>3</sub> in Raman and optical investigations at high pressure

Nelson Gross,<sup>1</sup> Yi-Yang Sun,<sup>2</sup> Samanthe Perera,<sup>1</sup> Haolei Hui,<sup>1</sup> Xiucheng Wei,<sup>1</sup> Shengbai Zhang,<sup>2</sup> Hao Zeng<sup>1</sup> and B. A. Weinstein<sup>1</sup>

<sup>1</sup>*Department of Physics, University at Buffalo, the State University of New York, Buffalo, NY 14260, USA*

<sup>2</sup>*Department of Physics, Applied Physics & Astronomy, Rensselaer Polytechnic Inst., Troy, NY 12180, USA*

We report experiments and calculations investigating the pressure and temperature dependences of the optical phonons in BaZrS<sub>3</sub>, and the pressure dependence of its absorption edge. BaZrS<sub>3</sub> is a chalcogenide perovskite in a novel class of materials being considered for photovoltaics. It is studied by Raman spectroscopy as functions of temperature (at 1 atm) and pressure (at 120K and 295K), and by pressure-transmission spectroscopy at 295K. Density functional theory (DFT) calculations predict the allowed Raman lines, their intensities, their pressure-shifts, and the band gap pressure-shift. Cooling shifts all but one of the phonon peaks to higher frequencies; the temperature coefficients are typical of semiconductors. A strong low-temperature peak at 392.3 cm<sup>-1</sup> is attributed to resonant forbidden LO scattering; its shift with temperature has the opposite sign. The pressure coefficients of the phonon frequencies for all observed Raman peaks are positive, indicating no mode softening. The rates of pressure shift also are typical, and show the customary scaling with phonon frequency. Experiment and theory show good agreement on the pressure-induced frequency shifts. The BaZrS<sub>3</sub> absorption edge moves to lower energy with pressure, reflecting reduction of the band gap. The measured shift is  $\sim -0.015$  eV/GPa, slightly less than the DFT result of  $-0.025$  eV/GPa. We find no evidence that the perovskite structure of BaZrS<sub>3</sub> undergoes any phase changes under hydrostatic pressure to at least 8.9 GPa. Our results indicate the robust structural stability of BaZrS<sub>3</sub>, and suggest cation alloying as a viable approach for band gap engineering for photovoltaic and other applications.

## Introduction

Chalcogenide perovskites containing group VI anions including S and Se are emerging as a novel class of semiconductors with potential photovoltaic and optoelectronic applications.[1-4] Although first synthesized some six decades ago,[5,6] these materials are scarcely investigated compared to their oxide counterparts, which have been studied intensively because of their geophysical significance,[7] and because of their ferroelectric, piezoelectric, electrolytic, and optoelectronic properties enabling many advances in applications.[8-13] The recent advances in organic-inorganic halide-perovskites as solar absorbers demonstrating power conversion efficiencies in the 20% range [14-16] has led to revived interests in chalcogenide perovskites,[1-4] in an effort to address the instability and toxicity issues faced by halide perovskites.

BaZrS<sub>3</sub> is a prototypical chalcogenide perovskite. It is theoretically predicted to be a direct band gap semiconductor with a band gap of  $\sim 1.7$ - $1.85$  eV. This is subsequently confirmed by optical measurement.[2-4] The material shows strong absorption in the visible spectrum. The material is also shown to be stable against oxidation and moisture.[3] For a single junction solar cell, the optimum band gap is 1.3-1.5 eV.[17] To tune the band gap of chalcogenide perovskites, cation or anion alloying can be employed. For example, full replacement of Ba in BaZrS<sub>3</sub> by Sr was shown to give a band gap  $\sim 2.1$  eV in  $\beta$ -SrZrS<sub>3</sub> (distorted perovskite phase) and  $\sim 1.5$  eV in  $\alpha$ -SrZrS<sub>3</sub> (needle-like phase)[4]. Also, by substitutionally replacing a fraction of the Zr in BaZrS<sub>3</sub> with Ti, the conduction band is expected to be lowered, thereby tuning the band gap to smaller energies. Since Ti has a smaller atomic radius, the volume of the unit cell is expected to shrink with increasing Ti concentration. It is therefore desirable to explore whether BaZrS<sub>3</sub> is structurally stable against volume compression.

In the present study, we employ Raman spectroscopy and density functional theory to investigate the pressure (P) and temperature (T) dependences of the optical phonons in this chalcogenide perovskite. Additionally, using optical transmission we show that the band gap of BaZrS<sub>3</sub> decreases with applied pressure, an important consideration for photovoltaics as noted above. Prior Raman studies on oxide perovskites[12,18-21] have established that knowledge of the effects of pressure and temperature on the vibrational modes is fundamental to understanding the structural stability, bonding, and polarization states in perovskites, and the mechanisms that mediate changes in these properties. The effects of pressure on the phonons and the band gap in BaZrS<sub>3</sub> have not been measured previously. A brief initial report of the low temperature Raman spectra of this material has appeared.[3] Prior reports of the Raman spectra at ambient conditions have been given for BaZrS<sub>3</sub>,[4,22] BaMS<sub>3</sub>

(M = Ti and Nb)[23], and SrZrS<sub>3</sub>[4] and the ambient band gaps of these materials have also been reported from experiment and theory.[1-4,22]

## Experiment

Polycrystalline powders of BaZrS<sub>3</sub> suitable for Raman measurements were grown by high-temperature sulfurization of BaZrO<sub>3</sub> ( $\geq 99\%$  purity) in a CS<sub>2</sub> atmosphere. CS<sub>2</sub> gas ( $\geq 99.8\%$  purity) was introduced to the sample via conventional Ar transport methods. The CS<sub>2</sub> flow rate (10-20 standard cm<sup>3</sup>/min), and the reaction time and temperature (~4h at 1050 °C) were optimized to obtain homogeneous BaZrS<sub>3</sub> without oxide phases or other impurity phases. The quality of the samples was confirmed by several characterization methods prior to our Raman experiments. Crystal structure and phase uniformity were assessed by X-ray (Cu K $\alpha$ ) diffraction (XRD) using a dual position graphite monochromator. The BaZrS<sub>3</sub> is found to be in the orthorhombic distorted perovskite *Pnma* structure with the lattice constants  $a = 7.04 \text{ \AA}$ ,  $b = 9.98 \text{ \AA}$ , and  $c = 7.05 \text{ \AA}$  in agreement with prior results.[6] Within the instrument's detection limits of 1% concentration, no secondary phase is observed. The morphology and elemental composition were analyzed using a field emission scanning electron microscope (SEM) equipped with an energy dispersive X-ray (EDX) spectrometer. A composition close to stoichiometry is found, with Ba : Zr : S proportions of 21.6 : 21.4 : 57.0. The small deviations from ABX<sub>3</sub> stoichiometry (a common situation in perovskites) probably arise from S-vacancies due to the high-temperature synthesis. The band gap is estimated to be 1.74 eV by UV-vis diffuse reflection spectroscopy. A detailed account of the BaZrS<sub>3</sub> synthesis and sample characterization results is presented elsewhere. [3]

Raman measurements were made using the 647 nm, 676 nm, and 752 nm lines of a CW Kr+ laser. The spectra were collected using a 1 m double monochromator (Jobin-Yvon U1000) equipped with 1800g/mm holographic gratings and a GaAs photomultiplier operating in photon counting mode. Because the samples were polycrystalline, polarized Raman spectra were not collected. Ambient pressure spectra were recorded at 295K-14K in a standard He closed-cycle cryostat. Spectra at high pressure were measured using ruby-calibrated diamond anvil cells (DAC) employing hardened stainless-steel gaskets with drilled sample chambers  $\sim 200\mu\text{m}\phi \times 70\mu\text{m}$  deep. We recorded Raman spectra at 295 K (RT) up to 8.9 GPa, and at 120K up to 6.8GPa. The pressure experiments at low temperature employed a separate liquid He variable temperature cryostat. The pressure medium in all the DAC runs was 4:1 methanol:ethanol. This alcohol medium is hydrostatic to 9.5 GPa at RT and quasi-hydrostatic in a gasketed DAC at low-T (*i.e.*, strain gradients of  $\lesssim 0.5$  GPa across the 200  $\mu\text{m}$  diameter gasket-sample-chamber).[24,25]

## DFT Calculations

First-principles calculations on the BaZrS<sub>3</sub> system were carried out based on density functional theory (DFT) using the PBEsol functional, [26] as implemented in the Vienna Ab-initio Simulation Package (VASP),[27] and projector augmented wave (PAW) potentials[28] were used together with a plane-wave basis set. Plane waves up to a kinetic energy cut off of 30 Ry were employed. A  $\Gamma$ -centered  $9\times 7\times 9$  k-point grid was used to sample the Brillouin zone. In structural optimization, the stopping criterion for atomic forces was set to be 0.2 mRy/Bohr. The lattice constants were optimized by using the calculated stress.[29] At the equilibrium volume, the calculated stress is smaller than 0.1 GPa. The calculations first obtained the equilibrium lattice constants and the internal atomic coordinates at  $P = 0$  GPa and  $T = 0$  K. The distorted perovskite structure with the *Pnma* space group [1] was used here. The optimized lattice constants found by the calculations are  $a = 7.102 \text{ \AA}$ ,  $b = 9.955 \text{ \AA}$ , and  $c = 6.957 \text{ \AA}$ , in good agreement with the experimental values from previous ( $a = 7.060 \text{ \AA}$ ,  $b = 9.981 \text{ \AA}$ , and  $c = 7.025 \text{ \AA}$ ) [30] and the present works. The calculated result for the bulk modulus of BaZrS<sub>3</sub> at  $P = 0$  is  $B_0 = 75$  GPa. To calculate  $B_0$ , we used the empirical equation of state proposed by Vinet et al.[31] and 9 data points for volume varying between about  $\pm 12.5\%$  of the equilibrium volume. To our knowledge, no measurements of  $B_0$  for this material have been reported.

We next calculated the frequencies  $\nu_i$  of the optical phonons using the linear response method [32] and the intensities of the Raman active modes following the method of Umari, *et. al.*[33] The pressure-shifts  $(d\nu_i/dP)_{P=0}$  of the phonon frequencies were then computed by reducing the volume from the ambient value  $V_0$  down to about  $0.913 V_0$  in six steps. At each reduced volume the lattice shape and the internal coordinates were re-optimized while preserving the reduced volume. Then the external pressure  $P$  and  $\nu_i$  were calculated at each reduced volume.

From our DFT calculations we also obtain the change in energy of the direct band gap with pressure. This is found to be approximately linear with an average shift to lower energy of  $\sim -0.025$  eV/GPa.

## Results

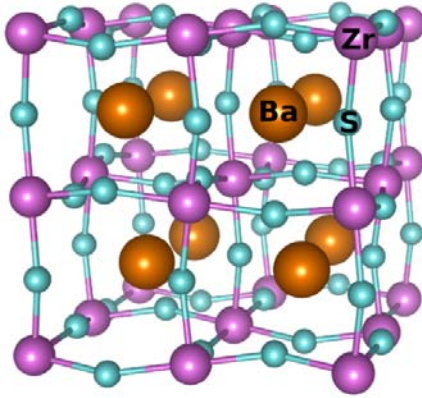


Fig. 1 BaZrS<sub>3</sub> distorted perovskite *Pnma* crystal structure.

Figure 1 shows the BaZrS<sub>3</sub> distorted perovskite structure. It has the orthorhombic space group *Pnma* ( $D_{2h}^{16}$ ) with four BaZrS<sub>3</sub> formula units per primitive unit cell. The lattice can be viewed as composed of distorted ZrS<sub>6</sub> corner-sharing octahedra, with each Ba atom centrally located in the spatial region defined by its neighboring S and Zr atoms. In this structural motif twisting of the ZrS<sub>6</sub> octahedra about the a-axis changes the symmetry from cubic to *Pnma*.<sup>[34]</sup>

Group theoretical analysis for the *Pnma* ( $D_{2h}^{16}$ ) structure reveals 57 zone-center optical phonons, classified according to  $(7A_g + 5B_{1g} + 7B_{2g} + 5B_{3g}) + (9B_{1u} + 7B_{2u} + 9B_{3u}) + 8A_u$ . Due to inversion symmetry, only the first 24 even (gerade) modes are Raman active. The next set of 25 odd-parity B-modes are infra-red active, and there are 8 optically inactive  $A_u$  modes.<sup>[35-37]</sup> Genet *et. al.*<sup>[38]</sup> have given diagrams of the mode geometries for this structure. Figure 2 presents the Raman spectrum of BaZrS<sub>3</sub> measured in this work at 14 K and  $P = 0$  for the spectral range

spanning the calculated intrinsic phonon frequencies of this material; the 676 nm laser line was used. Standard line-shape analysis (dashed and solid curves) is able to fit this spectrum with 16 peaks, and the labels designate the likely peak assignments. The vertical lines in the figure indicate the calculated positions and relative intensities of modes with theoretical relative oscillator strengths greater than 2%. Table I lists the symmetries and theoretical frequencies  $\nu_{o,th}$  of the 24 Raman active modes, and also gives the measured positions  $\nu_{o,ex}$  for the maxima of the fitted experimental peaks. In cases where the theoretical modes are too close to be experimentally resolved, identical experimental values of  $\nu_{o,ex}$  are given (five pairs of lines). We see

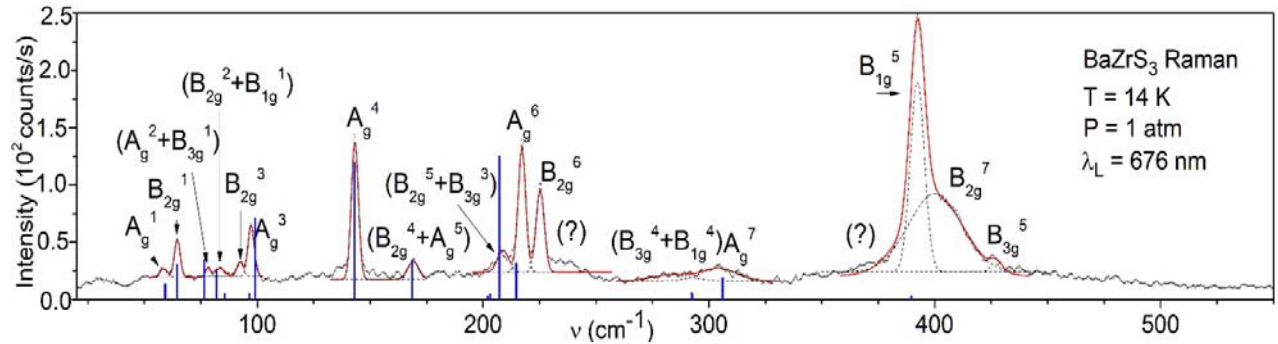


Fig. 2. Measured Raman spectrum (points) of BaZrS<sub>3</sub> at 14 K and  $P = 0$  GPa. Dashed and solid red curves are best fit results for the individual peaks and the cumulative spectrum, respectively. Labels give the peak phonon assignments based on comparison with the results of our DFT calculations. (See Table I, and text.) Question marks designate unassigned weak features that may arise from two-phonon scattering. Vertical lines indicate the theoretical strength of modes relative to the strongest DFT-calculated Raman peak ( $A_g^6$ -line at 206.8  $\text{cm}^{-1}$ ); calculated modes with theoretical strengths less than 2% of this maximum are not represented.

that the correspondence between experiment and theory for the frequencies and relative intensities of the spectral features observed below 325  $\text{cm}^{-1}$  is reasonably close. The predicted phonon frequencies are within 10  $\text{cm}^{-1}$  of the fitted peak maxima, and the relative intensities agree within 30%. The weak shoulders at 235  $\text{cm}^{-1}$  and at 378  $\text{cm}^{-1}$  (each marked by a (?)) may arise from two-phonon scattering, and these features are left unassigned at present.

The comparison is not as good between the  $B_{1g}^5$ ,  $B_{2g}^7$ , and  $B_{3g}^5$  modes and the measured peaks in the 390-440

Table I. Raman assignments with theoretical ( $\nu_{o,th}$ ) and fitted experimental ( $\nu_{o,ex}$ ) 14 K frequencies given in  $\text{cm}^{-1}$ . Adapted in part from Perera *et. al.*<sup>[3]</sup>

mode	$\nu_{o,th}$	$\nu_{o,ex}$	mode	$\nu_{o,th}$	$\nu_{o,ex}$	mode	$\nu_{o,th}$	$\nu_{o,ex}$	mode	$\nu_{o,th}$	$\nu_{o,ex}$
$A_g^1$	59.2	58.5	$B_{2g}^3$	97.7	92.4	$A_g^5$	168.6	169.0	$B_{3g}^4$	289.7	283.3
$B_{2g}^1$	64.0	64.6	$A_g^3$	98.9	97.2	$B_{1g}^3$	174.5		$B_{1g}^4$	290.2	283.3
$A_g^2$	76.0	78.2	$B_{1g}^2$	111.0		$B_{2g}^5$	201.7	208.9	$A_g^7$	304.0	304.3
$B_{3g}^1$	76.8	78.2	$A_g^4$	142.8	143.2	$B_{3g}^3$	202.9	208.9	$B_{1g}^5$	387.5	392.3
$B_{2g}^2$	81.6	83.4	$B_{3g}^2$	160.1		$A_g^6$	206.8	217.2	$B_{2g}^7$	398.6	400.1
$B_{1g}^1$	85.8	83.4	$B_{2g}^4$	167.7	169.0	$B_{2g}^6$	214.6	225.3	$B_{3g}^5$	417.6	426.5

$\text{cm}^{-1}$  region. Ishii *et al.*[22] show by a valence-force-field model that the phonons in this region correspond mainly to Zr-S stretching modes. We see in Figure 2 that the  $392.3 \text{ cm}^{-1}$  peak is the most intense feature in the 14 K Raman spectrum. This is at odds with the very weak oscillator strengths predicted by the DFT calculations for the  $B_{1g}^5$ ,  $B_{2g}^7$ , and  $B_{3g}^5$  modes, and so is puzzling. Also, the large width of the fitted peak at  $400 \text{ cm}^{-1}$  makes this feature difficult to assign. Although, its central frequency is close to that predicted for  $B_{2g}^7$ , the peak's large width suggests that it may arise from a mixture of unresolved features. In the next section we comment further on the scattering in the  $390\text{-}440 \text{ cm}^{-1}$  region.

In summary of the above results, based on the comparison between experiment and theory, we find that the most plausible assignments of the observed Raman peaks are those presented in Table I. All, but three, of the intrinsic phonon modes can be assigned.

### Temperature Dependence

The effect of temperature on the ambient pressure Raman spectrum of  $\text{BaZrS}_3$  was studied between 14 K and room temperature (RT). The recorded spectra are shown in Figure 3. The Raman peaks shift in frequency and sharpen upon cooling, and the sharpening enabled us to resolve four additional peaks ( $A_g^2, B_{2g}^4, B_{2g}^5, A_g^7$ ). The shift of all but one of the observed peaks is toward higher frequency with decreasing temperature, the characteristic behavior for anharmonic phonon interactions in semiconductors.[39,40] The exception is the anomalously strong peak at  $392.3 \text{ cm}^{-1}$  (Figure 3 and Table I). The observed maximum of this spectral feature moves in the opposite direction, to lower frequency with decreasing temperature.

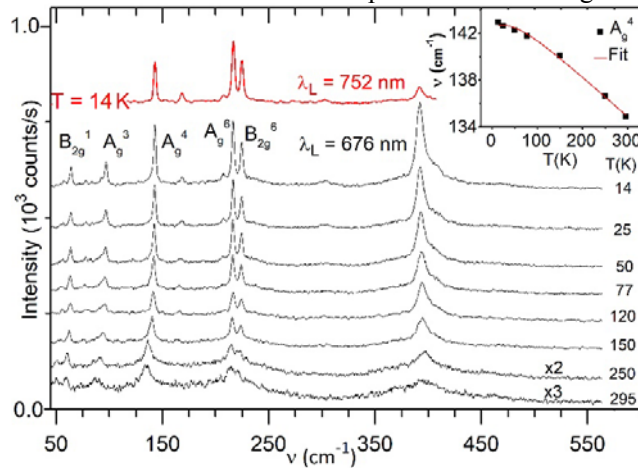


Fig 3.  $\text{BaZrS}_3$  Raman data taken at temperatures from 14 K to 295 K using 676 nm (lower eight traces) and 752 nm (top trace) laser lines. Spectra are displaced for clarity. The 752 nm trace is scaled individually as described in the text. The latter result shows the strong resonant Raman effect on the  $392.3 \text{ cm}^{-1}$  peak. Gaussian line shape fits are used to determine peak positions. Inset shows a sample fit of Eq. (1) to the temperature-shift of the  $A_g^4$  peak. Parameters for fit of Eq. (1) are given in Table II for all labeled peaks. Adapted in part from Perera *et al.*[3]

Both mechanisms contribute sums of terms that exhibit a

Table II. Fitted parameters in Eq. 1 that best describe  $\nu(T)$  for five of the prominent  $\text{BaZrS}_3$  Raman peaks in Figure 3. Fourth and fifth columns give the quality of fit  $R^2$  and the limiting high-T slopes, respectively.

mode	$\nu_o$ [ $\text{cm}^{-1}$ ]	$\nu_{av}$ [ $\text{cm}^{-1}$ ]	$\Delta$ [ $\text{cm}^{-1}$ ]	$R^2$	high-T slope [ $\text{cm}^{-1}/\text{K}$ ]
$B_{2g}^1$	64.6	57.9	0.72	0.996	-0.0173
$A_g^3$	98.2	63.2	1.25	0.999	-0.0275
$A_g^4$	145.6	116.2	2.92	0.994	-0.0349
$A_g^6$	217.1	93.1	0.68	0.966	-0.0101
$B_{2g}^6$	226.2	152.8	1.75	0.982	-0.0159

Figure 3 allows us to follow the evolution of the intensity of the anomalous  $392.3 \text{ cm}^{-1}$  peak for Raman spectra recorded with the 676 nm laser line. With decreasing temperature this sharp peak rises rapidly out of the broad

behavior for anharmonic phonon interactions in semiconductors.[39,40] The exception is the anomalously strong peak at  $392.3 \text{ cm}^{-1}$  (Figure 3 and Table I). The observed maximum of this spectral feature moves in the opposite direction, to lower frequency with decreasing temperature.

$$\nu(T) = \nu_o - \Delta[1 + 2n(\nu_{av}, T)] \quad (1)$$

where  $\nu_o$  is the harmonic frequency at  $T = 0 \text{ K}$ ,  $\Delta$  is the  $T = 0 \text{ K}$  renormalization due to disorder effects (*e.g.*, isotope disorder, impurities, defects),  $n$  is the Bose-Einstein population function, and  $\nu_{av}$  is an average interaction frequency. This expression jointly includes the contribution of 3-phonon decay (the dominant multi-phonon process), and the effect of thermal expansion.  $T$ -dependence similar to that in Eq. 1; the fitted value of  $\nu_{av}$  accounts for these sums in an average way.

In our experimental data six modes could be traced up to 295K, including the anomalous  $392.3 \text{ cm}^{-1}$  feature that shifts to lower frequency with decreasing  $T$ . Table II gives the parameters found from the best fits of Eq. 1 for the five modes that exhibit the usual type of behavior. The dependence at high- $T$  is linear with negative slopes (last column of Table II), and the dependence for these modes tends to become sub-linear in the range 40-60 K. The values of  $\Delta$  and  $\nu_{av}$  are typical of those in other semiconductor materials.[41,42]

feature seen at 295 K in the 390-440  $\text{cm}^{-1}$  region, and below 50 K, the 392.3  $\text{cm}^{-1}$  peak is the most intense peak in the spectrum. Its frequency shift over the temperature range 14-150 K (where its position is not strongly up-shifted by the broad peak at higher frequency) is approximately linear with a slope of  $\sim +0.018 \text{ cm}^{-1}/\text{K}$ . A satisfactory fit of Eq. 1 to the T-dependence of the anomalous 392.3  $\text{cm}^{-1}$  peak cannot be obtained. Eq. 1 approaches  $T = 0 \text{ K}$  with vanishing slope, whereas the frequency of the 392.3  $\text{cm}^{-1}$  peak asymptotes toward  $T = 0 \text{ K}$  with a positive slope.

To further explore the anomalously strong scattering in the 390-440  $\text{cm}^{-1}$  region, Raman data were collected using 752 nm (1.65 eV) excitation. The top spectrum in Fig. 3 gives the 14K result, with the intensity scaled so that the height of the  $A_g^6$  peak matches that of the same peak in the second upper-most trace measured at 14K using 676 nm (1.83 eV). Comparing these two spectra, we see that the relative intensity of the 390-440  $\text{cm}^{-1}$  scattering, particularly the 392.3  $\text{cm}^{-1}$  peak, is much reduced for 752 nm excitation. This strongly suggests that resonant forbidden LO-phonon scattering is the most likely cause of the 390-440 $\text{cm}^{-1}$  anomaly.[43] Such scattering (due to the Frohlich mechanism) undergoes a much stronger resonant enhancement than allowed scattering. Because 752 nm falls in the transparent region below the band gap of our  $\text{BaZrS}_3$  powder sample ( $E_g \sim 1.74 \text{ eV}$ ), whereas 676 nm is resonant with the interband transitions, forbidden scattering is expected to contribute more strongly to spectra recorded with the latter line than with the former. The forbidden scattering is aided by the mixture of crystallite geometries available to support this process in our powder sample; the usual selection rules are relaxed due to the  $\mathbf{q}$ -dependence of the Frohlich electron-phonon mechanism.

### Pressure Dependence

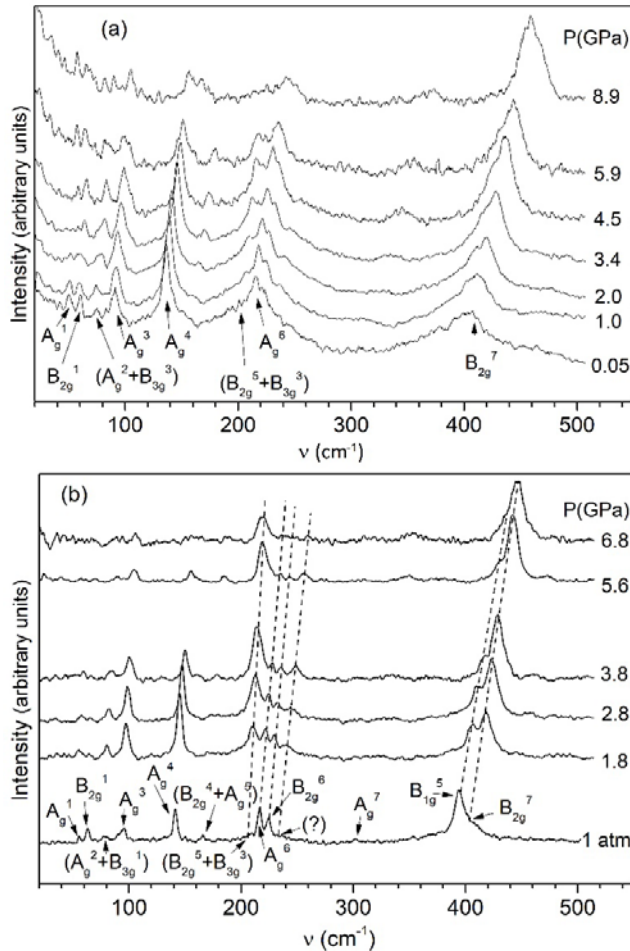


Fig 4. Pressure-Raman spectra of  $\text{BaZrS}_3$  recorded with the 647 nm laser line at a) 295 K, and b) 120 K. Spectra are displaced for clarity. Phonon assignments are given for the peaks that can be followed with pressure. Feature marked by (?) is unassigned (see text). Dashed lines are guides to the eye showing shift of closely spaced peaks.

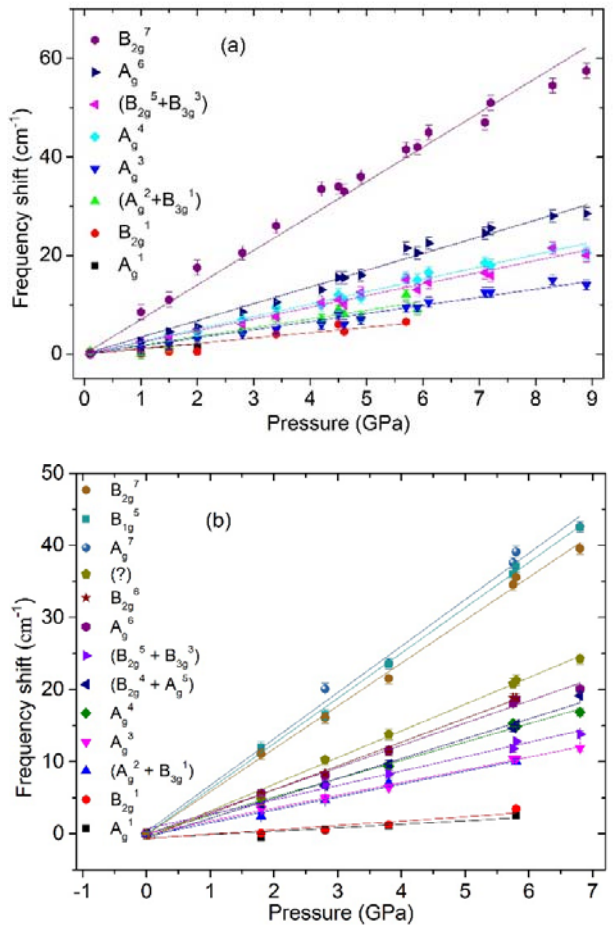


Fig 5. Frequency shifts with pressure of the observed Raman peaks in Figure 4 for a) 295K, and b) 120K. Peak positions are determined by Gaussian line shape fits. The mode correspondence of the plots follows the legends at left. The lines show the best linear fits to the data points.

The effects of applied pressure on the Raman spectrum of BaZrS<sub>3</sub> were investigated at two different temperatures. Figure 4(a) shows several spectra recorded from 0.05 GPa to 8.9 GPa at 295 K; Figure 4(b) presents spectra recorded at 120 K for various pressures up to 6.8 GPa. The pressure-Raman experiments conducted at 120 K were able to exploit the low-temperature sharpening of the spectra, thereby resolving more peaks and tracking their pressure dependences with greater precision. In both sets of data, we find that all of the observed peaks shift to higher frequency (*i.e.*, phonon stiffening) with increasing pressure. In addition, the Raman intensity of the overall spectrum tends to decrease gradually as the pressure is raised. This change is smaller for the scattering in the 390-440 cm<sup>-1</sup> region which becomes more prominent at high pressure. However, no new peaks appear in the high-pressure spectra, and the changes in frequency and intensity *occur continuously*. Consequently, we conclude that there is no evidence for any first-order structural phase changes in BaZrS<sub>3</sub> under hydrostatic pressure up to the maximum of 8.9 GPa studied here. We can expect this lower pressure bound to apply also at reduced temperature even though our 120 K data extend only to 6.8 GPa. For these types of first-order transitions, the main result of decreasing temperature is to make the kinetics more sluggish without having a sensitive effect on the equilibrium phase boundary.[21,44]

Figures 5(a) and 5(b) plot the shifts of the peak positions of the Raman lines that could be accurately followed as a function of pressure at 295 K and 120 K, respectively. All of the peaks exhibit linear pressure shifts within experimental uncertainty. Furthermore, there appears to be no hysteresis in the pressure shifts, as data recorded for both increasing and decreasing pressure lie along the same best-fit lines. The lack of hysteresis also supports the absence of a first order structure transition in the studied pressure range. The pressure coefficients (dv/dp)<sub>ex</sub> found from the slopes of the linear fits to the data at 120 K are tabulated in Table III. The pressure coefficients at 295 K exhibit a similar mode pressure dependence, but tend to be an average of ~13% larger. At present the reason for this deviation is unclear; it may be that the compressibility is larger at room temperature than at 120 K, but this needs further investigation. However, we regard the 120 K data as the more accurate due to the sharpening of the spectra at low-temperature. Moreover the 120K data give a fairer comparison to the theory, since the DFT results are calculated for T = 0 K.

In Table III, we also list for comparison the linear pressure coefficients predicted for the BaZrS<sub>3</sub> modes by our DFT calculations, as well as the Gruneisen constants  $\gamma = -B_0(d\ln(v)/dp)_{p=0}$  computed from both the measured and calculated pressure coefficients using  $B_0 = 75$  GPa, our DFT-calculated value for the bulk modulus. Generally, the agreement between experiment and theory for the pressure coefficients is quite good. The largest differences (~33%) are for the (B<sub>2g</sub><sup>4</sup>+A<sub>g</sub><sup>5</sup>) and (B<sub>2g</sub><sup>5</sup>+B<sub>3g</sub><sup>3</sup>) modes, and the latter is difficult to resolve in the measurements because of its close proximity to the intense A<sub>g</sub><sup>6</sup> peak. Otherwise, the theoretical pressure coefficients fall within  $\pm 20\%$  of the corresponding measured rates of shift, which themselves have an uncertainty of  $\pm 15\%$ .

Table III. Phonon pressure coefficients in cm<sup>-1</sup>/GPa, and corresponding Gruneisen parameters  $\gamma$ , observed experimentally (ex) at 120 K and calculated by DFT theory (th) in the present work. The DFT-calculated bulk modulus  $B_0 = 75$  GPa is used for all  $\gamma$ -values. Intrinsic BaZrS<sub>3</sub> modes are identified by their symmetry assignments. The mode labeled by (?), corresponding to the similarly marked feature in Figure 4b, may be due to two-phonon scattering.

mode	$\left.\frac{dv}{dP}\right _{ex}$	$\left.\frac{dv}{dP}\right _{th}$	$\gamma_{ex}$	$\gamma_{th}$	mode	$\left.\frac{dv}{dP}\right _{ex}$	$\left.\frac{dv}{dP}\right _{th}$	$\gamma_{ex}$	$\gamma_{th}$	mode	$\left.\frac{dv}{dP}\right _{ex}$	$\left.\frac{dv}{dP}\right _{th}$	$\gamma_{ex}$	$\gamma_{th}$
A <sub>g</sub> <sup>1</sup>	0.6	0.8	0.8	1.0	A <sub>g</sub> <sup>4</sup>	2.5	2.4	1.3	1.3	(?)	3.7		1.2	
B <sub>2g</sub> <sup>1</sup>	0.8	1.0	1.0	1.2	B <sub>3g</sub> <sup>2</sup>		2.3		1.1	B <sub>3g</sub> <sup>4</sup>		7.6		1.9
A <sub>g</sub> <sup>2</sup>	1.8	1.7	1.7	1.7	B <sub>2g</sub> <sup>4</sup>	2.8	3.8	1.2	1.7	B <sub>1g</sub> <sup>4</sup>		6.5		1.7
B <sub>3g</sub> <sup>1</sup>	1.8	1.9	1.7	1.8	A <sub>g</sub> <sup>5</sup>	2.8	2.2	1.2	1.0	A <sub>g</sub> <sup>7</sup>	6.4	7.5	1.5	1.8
B <sub>2g</sub> <sup>2</sup>		1.4		1.3	B <sub>1g</sub> <sup>3</sup>		4.3		1.8	B <sub>1g</sub> <sup>5</sup>	6.3	5.3	1.2	1.0
B <sub>1g</sub> <sup>1</sup>		1.4		1.2	B <sub>2g</sub> <sup>5</sup>	2.0	2.4	0.7	0.9	B <sub>2g</sub> <sup>7</sup>	5.9	5.7	1.1	1.1
B <sub>2g</sub> <sup>3</sup>		2.2		1.7	B <sub>3g</sub> <sup>3</sup>	2.0	3.6	0.7	1.3	B <sub>3g</sub> <sup>5</sup>		5.6		1.0
A <sub>g</sub> <sup>3</sup>	1.8	1.5	1.4	1.1	A <sub>g</sub> <sup>6</sup>	3.1	3.4	1.1	1.2					
B <sub>1g</sub> <sup>2</sup>		3.5		2.4	B <sub>2g</sub> <sup>6</sup>	3.3	3.6	1.1	1.3					

## Discussion

We have found that the most likely source of the unexpectedly strong Raman features at 390-440  $\text{cm}^{-1}$ , dominated by the 392.3  $\text{cm}^{-1}$  peak for  $T < 50$  K, is resonant forbidden LO scattering aided by the mix of crystallite geometries in our powder sample that can support this process. Recently, forbidden LO scattering also was proposed to explain the presence of unexpected strong Raman peaks in the spectra of the halide perovskites  $\text{CsSnX}_3$  ( $X = \text{I}, \text{Br}, \text{Cl}$ ).[45,46]

Several other explanations are much less probable. Our samples are grown by sulfurization of  $\text{BaZrO}_3$  in  $\text{CS}_2$ , so at first sight one might expect O impurities to be a possible source of the anomalous scattering. However, a broad peak having similar strength and shape is seen at a comparable location in recent Raman results (room temperature) on  $\text{BaZrS}_3$  grown directly from BaS, Zr, and S.[4] Hence, it is doubtful that the strong intensity of the 390-440  $\text{cm}^{-1}$  scattering can be explained by O impurities. Also unlikely is an explanation based on the presence of other Ba-Zr-S phases, such as  $\text{Ba}_2\text{ZrS}_4$  and  $\text{Ba}_3\text{Zr}_2\text{S}_7$  which have a partially overlapping Raman band in the 400-500  $\text{cm}^{-1}$  range.[22] The XRD characterization of our material shows that these phases could at most make up 1% of the sample.[3] Accordingly, one does not expect that their Raman contributions would be sufficient to explain the 390-440  $\text{cm}^{-1}$  scattering. We might also consider the involvement of two-phonon scattering.[22] However, in order for second-order processes to be responsible for the 392.3  $\text{cm}^{-1}$  peak, they would need to give rise to the most intense feature in the spectrum at low temperatures, and this is again problematic. As remarked, the weak shoulders in Figure 2 at 235  $\text{cm}^{-1}$  and 378  $\text{cm}^{-1}$  (marked by (?)) are possible two-phonon features. Under pressure (Figure 4(b)), the former becomes a more defined peak as it separates from  $B_{2g}^6$ , but the latter shoulder does not become separately resolved from the stronger peaks in the 390-440  $\text{cm}^{-1}$  region. The interesting behavior of the 390-440  $\text{cm}^{-1}$  Raman features warrants additional future study.

We also find that the overall intensity of the Raman spectrum weakens with increasing pressure. A pressure-shift of the band gap to lower energy is the most likely reason. This is predicted by our DFT calculations, which find that the band gap of  $\text{BaZrS}_3$  is a direct gap with a negative pressure coefficient of  $\sim -0.025$  eV/GPa. The observed Raman weakening reflects the enhanced attenuation of the incident and scattered photons due to the increase in absorption brought on by the down-shift of the band gap energy with pressure.

To explore this further a study was carried out on the pressure dependence of the absorption edge in a  $\text{BaZrS}_3$  film sample at 295 K. Films suitable for transmission measurements in the DAC were grown by pulsed laser ablation of  $\text{BaZrO}_3$  on sapphire followed by high-temperature sulfurization in  $\text{CS}_2$ . The growth conditions and characterization were similar to our powder sample. Good quality films were obtained, again showing the  $Pnma$   $\text{BaZrS}_3$  structure and composition near stoichiometry. The substrate was thinned to  $\sim 45\mu\text{m}$  to prevent pinching in the DAC. Data were recorded to 8.1 GPa on a  $\sim 60$  nm thick film. The findings are summarized in Fig. 6 in which

the spectra are represented in a plot of  $(E \cdot \alpha)^2$  vs  $E$ , with  $\alpha$  the absorbance. The pressure-induced energy shift  $\Delta E_g$  of the band gap can be estimated by noting the change in the extrapolated zero-crossings of the plotted absorption edges (dashed lines), according to the standard  $E$ -dependence in a direct gap material.[47] We see that a slightly higher ( $\sim 0.1$  eV) estimate of the ambient gap is indicated in the film compared to the diffuse reflectance result for our powder material ( $E_g = 1.74$  eV). This difference is attributed to the film's  $\sim 60$  nm thickness which permits us to observe only the upper portion of the edge. Also in the DAC film experiments scattered light contributes some uncertainty to the data. Nevertheless, a reasonable estimate of the band-gap *pressure-shift*  $\Delta E_g$  (Fig. 6 inset) can be obtained by means of this extrapolation procedure, *applied consistently* at each pressure. Our experimental results confirm the DFT-predicted trend that applied hydrostatic pressure reduces the band gap of  $\text{BaZrS}_3$ . The measured change for the total applied pressure of

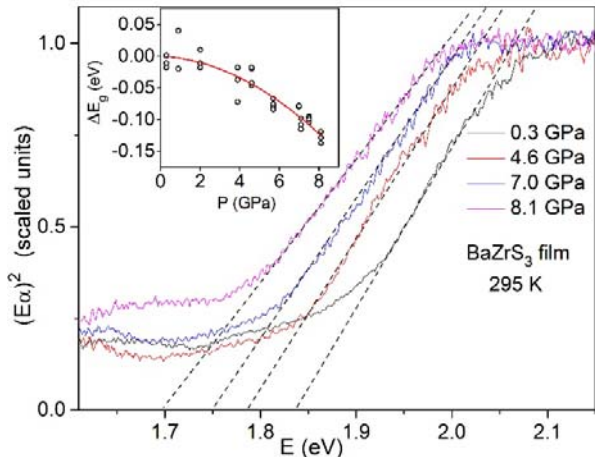


Fig. 6. Measured effect of pressure on the band edge of  $\text{BaZrS}_3$ . Spectra are plotted as  $(E\alpha)^2$  vs  $E$ ;  $\alpha$  is the absorbance. Spectra are scaled vertically to match heights in the plateau region above 2.1 eV, and no reflectivity correction is made. Dashed lines extrapolate the edges to zero in order to estimate the pressure variation of the band gap in a consistent way. Inset shows the band gap energy-shift  $\Delta E_g$  vs pressure with a quadratic fit to the data.



8.1 GPa amounts to an average of roughly  $-0.015$  eV/GPa, a bit less than the rate of shift found in our DFT calculations, and some non-linearity in the measured pressure shift is observed. Reduction of the BaZrS<sub>3</sub> band gap under applied pressure is a favorable result for photovoltaic applications. This will be discussed further below.

The overall weakening of the Raman intensity might also be attributed to a progressive pressure-driven twisting of the S-octahedra toward the ideal cubic perovskite phase; its cubic structure does not allow a first-order Raman effect. We can rule this out because it violates trends seen in oxide perovskites where the opposite behavior occurs. For example in the BaCe<sub>x</sub>Zr<sub>1-x</sub>O<sub>3</sub> system, pressure twists the O-octahedra toward lower symmetry phases; the sequence with increasing pressure is cubic to rhombohedral to two different orthorhombic phases, the last being the *Pnma* structure.[21] Subsequent phase transitions to more complicated closer packed structures occur at significantly higher pressures.[20]

As remarked, there is no evidence from our experiments that the distorted perovskite *Pnma* structure of BaZrS<sub>3</sub> undergoes any first order phase changes under hydrostatic pressure up to at least 8.9 GPa. None of the measured or calculated phonon frequencies in BaZrS<sub>3</sub> soften under applied pressure (no negative pressure coefficients), further supporting the structural stability against compression. This result is also found in a variety of oxide perovskites,[7,12,21] and the robustness of the BaZrS<sub>3</sub> *Pnma* phase under pressure conforms to the structural trends for those perovskites alluded to above. Therefore, the results of our work indicate that over a considerable span of pressures, the crystal structure of BaZrS<sub>3</sub> is robust and stable against compression in its *Pnma* phase.

This robustness is an issue of some importance for photovoltaic and other applications. It suggests that band-gap tuning in the *Pnma* phase based on cation alloying of BaZrS<sub>3</sub> with other metals such as Ca, Sr, Ti, etc. should be possible for a wide range of compositions. In particular, if Zr<sup>4+</sup> is partially substituted by Ti<sup>4+</sup>, the 3d orbitals of Ti<sup>4+</sup> will lead to a downward shift of the conduction band minimum, and lower the band gap.[2] This can in turn result in optimal matching of the band gap of this material with the solar spectrum for photovoltaic applications. Our BaZrS<sub>3</sub> powder material has a band gap of  $\sim 1.74$  eV as determined by diffuse reflectance spectroscopy.[3] This is slightly higher than the optimum value of 1.3-1.5 eV required for a single junction solar cell. Since the spatial size of Ti<sup>4+</sup> is considerably smaller than that of Zr<sup>4+</sup>, (e.g., the ionic radius is  $\sim 12\%$  smaller) Ti alloying will lead to compression of the lattice. Studying the phase stability of BaZrS<sub>3</sub> under high pressure can provide crucial information for feasible doping concentrations.

Our DFT calculations for the compression of BaZrS<sub>3</sub> by hydrostatic pressure find that at 10.7 GPa the *Pnma* unit cell volume of BaZrS<sub>3</sub> corresponds to the unit cell volume that we calculate for BaTiS<sub>3</sub> in the analogous *Pnma* structure at  $P = 0$  GPa. These results suggest that BaZr<sub>1-x</sub>Ti<sub>x</sub>S<sub>3</sub> should be able to accommodate high concentrations of Ti as judged from the apparent robustness found here for the *Pnma* phase under compression by hydrostatic pressure alone to 8.9 GPa.

Work based on first principles calculation for the BaZr<sub>1-x</sub>Ti<sub>x</sub>S<sub>3</sub> alloy system predicted that phase-separation into BaZrS<sub>3</sub> and BaTiS<sub>3</sub> is favored because of entropy effects when  $x$  is above 0.1.[2] Early attempts to incorporate Ti were unsuccessful possibly due to low synthesis temperature, not necessarily due to thermodynamics. At high alloy concentration BaZr<sub>1-x</sub>Ti<sub>x</sub>S<sub>3</sub> material does phase-separate, however, an experimental study reported stable single phase BaZr<sub>0.75</sub>Ti<sub>0.25</sub>S<sub>3</sub> synthesized under high pressure (6 GPa) high temperature (900 C) conditions.[48] Future work is needed to explore the limits of metal alloying in perovskites based on BaZrS<sub>3</sub>. Nevertheless, Ti-alloying can be expected to be a viable means for reducing the band gap toward values closer to the optimal range for solar absorption with accompanying increases in power conversion efficiency.[2] Our own preliminary experiments are promising, indicating that a small alloy concentration of  $\sim 5\%$  Ti is effective in reducing the gap by amounts on the order of the full 8.9 GPa shift in Fig. 6. Alloying with other cations could lead to wide tunability of the band gap, e.g. Ca<sup>2+</sup> substituting Ba<sup>2+</sup> can increase the band gap,[3] which can enable other optoelectronic applications. The focus of the present investigation is on high pressure optical studies of BaZrS<sub>3</sub>, and a study of Ti-alloying itself will be presented elsewhere.

The effects of pressure on the phonon frequencies in BaZrS<sub>3</sub> reflect a stable solid that obeys the quasi-harmonic approximation. This behavior is typical in inorganic perovskites. [7,12,21] The phonon pressure shifts in BaZrS<sub>3</sub> (Figure 5 and Table III) scale in proportion to the mode frequencies. Zallen and Slade[49] have shown that such scaling holds for solids with a single bonding type, and can be expected in ionic and covalent solids, but not in molecular crystals. The scaling of the pressure-shifts means that the fractional rates of shift for the different phonon frequencies are approximately similar. The extent of this similarity is gauged by the range of the Gruneisen parameters. From Table III we see that the experimental and calculated Gruneisen parameters vary,

respectively, between 0.7 – 1.7 and 0.9 – 1.9 (except  $\gamma_{\text{calc}} = 2.4$  for the  $B_{1g}^2$  mode), and within these ranges the mode dependence for both sets of values is similar. Overall the agreement between experiment and theory for the phonon pressure coefficients (and  $\gamma$  values) is quite good.

### Summary

This work has reported experimental and theoretical studies of the Raman active phonons and the band gap absorption edge in  $\text{BaZrS}_3$ , focusing on the effects of high pressure, and for the phonons also low temperature. DFT calculations predict the frequencies, relative intensities, and pressure-shifts of the 24 allowed Raman lines at 0 K, as well as compute the pressure dependence of the band gap. We have been able to assign 21 of the 24 intrinsic Raman-active phonons to observed spectral peaks. The agreement with theory of the measured frequencies and intensities is excellent except for the stronger than expected features observed in the 390-440  $\text{cm}^{-1}$  region which include a puzzling sharp peak at 392.3  $\text{cm}^{-1}$ . These anomalous features can be attributed to resonant forbidden Raman scattering driven by the Frohlich mechanism. Residual O impurities, other Ba-Zr-S phases, and two-phonon scattering are ruled out as likely causes. The measured temperature coefficients of the phonon frequencies have typical negative values, except for the 392.3  $\text{cm}^{-1}$  peak. The unusual temperature-shift of this peak is not yet understood. With increasing pressure all measured Raman peaks shift linearly to higher frequency, revealing *no mode softening*. The rates of pressure shift are characteristic of inorganic perovskites, and scale with frequency as expected for a quasi-harmonic solid. The calculated pressure-coefficients of the intrinsic phonon modes agree closely with experiment. Measurements of the effects of pressure on the  $\text{BaZrS}_3$  absorption edge find that the band gap shifts to lower energy at a rate of  $\sim -0.015$  eV/GPa. This agrees in sign, but is smaller than, the theoretical shift of  $-0.025$  eV/GPa predicted by our DFT calculations. There is no evidence that the distorted perovskite *Pnma* crystal structure of  $\text{BaZrS}_3$  undergoes a structural phase transitions under hydrostatic pressure to *at least* 8.9 GPa in our experiments. This apparent stability suggests that band-gap engineering by adding appropriate metals in alloys based on the  $\text{BaZrS}_3$  *Pnma* phase should be explored for photovoltaic and other applications.

### Acknowledgments

Work supported by NSF DMR-1104994, CBET-1510121, CBET- 1510948, MRI-1229208, and DOE DE-EE0007364. We thank W.R.L. Lambrecht for suggesting the possible role of the resonant forbidden Raman effect.

### References

- [1] Y.-Y. Sun, M. L. Agiorgousis, P. Zhang, and S. Zhang, Chalcogenide Perovskites for Photovoltaics, *Nano Lett.* **15**, 581 (2015).
- [2] W. Meng, B. Saparov, F. Hong, J. Wang, D. B. Mitzi, and Y. Yan, Alloying and Defect Control within Chalcogenide Perovskites for Optimized Photovoltaic Application, *Chem. Mater.* **28**, 821 (2016).
- [3] S. Perera, H. Hui, C. Zhao, H. Xue, F. Sun, C. Deng, N. Gross, C. Milleville, X. Xu, D. F. Watson, B. A. Weinstein, Y.-Y. Sun, S. Zhang, and H. Zeng, Chalcogenide perovskites—an emerging class of ionic semiconductors, *Nano Energy* **22**, 129 (2016).
- [4] S. Niu, H. Huyan, Y. Liu, M. Yeung, K. Ye, L. Blankemeier, T. Orvis, D. Sarkar, D. J. Singh, R. Kapadia, and J. Ravichandran, Bandgap Control via Structural and Chemical Tuning of Transition Metal Perovskite Chalcogenides, *Adv. Mater.* **29**, 1604733 (2017).
- [5] H. Hahn and U. Mutschke, Untersuchungen über ternäre Chalkogenide. XI. Versuche zur Darstellung von Thioperovskiten, *Z. Anorg. Allg. Chem.* **288**, 269 (1957).
- [6] A. Clearfield, The synthesis and crystal structures of some alkaline earth titanium and zirconium sulfides, *Acta Crystallogr.* **16**, 135 (1963).
- [7] R. J. Hemley and R. E. Cohen, Silicate Perovskite, *Annu. Rev. Earth Planet Sci.* **20**, 553 (1992).
- [8] N. A. Hill, Why Are There so Few Magnetic Ferroelectrics?, *J. Phys. Chem. B* **104**, 6694 (2000).
- [9] J. F. Scott, The physics of ferroelectric ceramic thin films for memory applications, *Ferroelectr. Rev.* **1**, 1 (1998).
- [10] A. J. Millis, Lattice effects in magnetoresistive manganese perovskites, *Nature* **392**, 147 (1998).
- [11] C. D. Chandler, C. Roger, and M. J. Hampden-Smith, Chemical aspects of solution routes to perovskite-phase mixed-metal oxides from metal-organic precursors, *Chem. Rev.* **93**, 1205 (1993).
- [12] M. Ahart, R. E. Cohen, V. Struzhkin, E. Gregoryanz, D. Rytz, S. A. Prosandeev, H. K. Mao, and R. J. Hemley, High-pressure Raman scattering and x-ray diffraction of the relaxor ferroelectric 0.96  $\text{Pb}(\text{Zn}_{1/3}\text{Nb}_{2/3})\text{O}_3$ -0.04  $\text{PbTiO}_3$ , *Phys. Rev. B* **71**, 144102 (2005).
- [13] A. Kojima, K. Teshima, Y. Shirai, and T. Miyasaka, Organometal Halide Perovskites as Visible-Light Sensitizers for Photovoltaic Cells, *J. Am. Chem. Soc.* **131**, 6050 (2009).
- [14] T. Zhang, M. Yang, Y. Zhao, and K. Zhu, Controllable sequential deposition of planar  $\text{CH}_3\text{NH}_3\text{PbI}_3$  perovskite films via adjustable volume expansion, *Nano Lett.* **15**, 3959 (2015).
- [15] C. Bi, Q. Wang, Y. Shao, Y. Yuan, Z. Xiao, and J. Huang, Non-wetting surface-driven high-aspect-ratio crystalline grain growth for efficient hybrid perovskite solar cells, *Nat. Commun.* **6**, 7747 (2015).

- [16] W. Nie, H. Tsai, R. Asadpour, J. C. Blancon, A. J. Neukirch, G. Gupta, J. J. Crochet, M. Chhowalla, S. Tretiak, M. A. Alam, H. L. Wang, and A. D. Mohite, High-efficiency solution-processed perovskite solar cells with millimeter-scale grains, *Science* **347**, 522 (2015).
- [17] W. Shockley and H. J. Queisser, Detailed balance limit of efficiency of p-n junction solar cells, *J. Appl. Phys.* **32**, 510 (1961).
- [18] R. J. Hemley, R. E. Cohen, A. Yeganeh-Haeri, H. K. Mao, D. J. Weidner, and E. Ito, Raman spectroscopy and lattice dynamics of MgSiO<sub>3</sub>-perovskite at high pressure, in: *Geophysical Monograph Series* Vol. **45**, 35 (1989).
- [19] H. K. Mao, R. J. Hemley, Y. Fei, J. F. Shu, L. C. Chen, A. P. Jephcoat, Y. Wu, and W. A. Bassett, Effect of pressure, temperature, and composition on lattice parameters and density of (Fe, Mg) SiO<sub>3</sub>-perovskites to 30 GPa, *J. Geophys. Res.* **96**, 8069 (1991).
- [20] S. Loidant and G. Lucazeau, High-pressure Raman study of the perovskite BaCeO<sub>3</sub>, *J. Raman Spectrosc.* **30**, 485 (1999).
- [21] C. Chemarin, N. Rosman, T. Pagnier, and G. Lucazeau, A high-pressure raman study of mixed perovskites BaCe<sub>x</sub>Zr<sub>1-x</sub>O<sub>3</sub> (0 ≤ x ≤ 1), *J. Solid State Chem.* **149**, 298 (2000).
- [22] M. Ishii, M. Saeki, and M. Sekita, Vibrational spectra of barium-zirconium sulfides, *Mater. Res. Bull.* **28**, 493 (1993).
- [23] M. Ishii and M. Saeki, Raman and infrared spectra of BaTiS<sub>3</sub> and BaNbS<sub>3</sub>, *Phys. Status Solidi B* **170**, K49 (1992).
- [24] B. A. Weinstein, Ruby thermometer for cryobaric diamond-anvil cell, *Rev. Sci. Instrum.* **57**, 910 (1986).
- [25] R. J. Angel, M. Bujak, J. Zhao, G. D. Gatta, and S. D. Jacobsen, Effective hydrostatic limits of pressure media for high-pressure crystallographic studies, *J. Appl. Crystallogr.* **40**, 26 (2007).
- [26] J. P. Perdew, A. Ruzsinszky, G. I. Csonka, O. A. Vydrov, G. E. Scuseria, L. A. Constantin, X. Zhou, and K. Burke, Restoring the Density-Gradient Expansion for Exchange in Solids and Surfaces, *Phys. Rev. Lett.* **100**, 136406 (2008).
- [27] G. Kresse and J. Furthmüller, Efficiency of ab-initio total energy calculations for metals and semiconductors using a plane-wave basis set, *Comput. Mater. Sci.* **6**, 15 (1996).
- [28] G. Kresse and D. Joubert, From ultrasoft pseudopotentials to the projector augmented-wave method, *Phys. Rev. B* **59**, 1758 (1999).
- [29] O. H. Nielsen and R. M. Martin, Quantum-mechanical theory of stress and force, *Phys. Rev. B* **32**, 3780 (1985).
- [30] R. Lelieveld and D. Ijdo, Sulphides with the GdFeO<sub>3</sub> structure, *Acta Crystallogr. B* **36**, 2223 (1980).
- [31] P. Vinet, J. H. Rose, J. Ferrante, and J. R. Smith, Universal features of the equation of state of solids, *J. Phys. Condens. Matter* **1**, 1941 (1989).
- [32] S. Baroni, S. De Gironcoli, A. Dal Corso, and P. Giannozzi, Phonons and related crystal properties from density-functional perturbation theory, *Rev. Mod. Phys.* **73**, 515 (2001).
- [33] P. Umari, A. Pasquarello, and A. Dal Corso, Raman scattering intensities in α-quartz: A first-principles investigation, *Phys. Rev. B* **63**, 094305 (2001).
- [34] J. A. Brehm, J. W. Bennett, M. R. Schoenberg, I. Grinberg, and A. M. Rappe, The structural diversity of ABS<sub>3</sub> compounds with d<sup>0</sup> electronic configuration for the B-cation, *J. Chem. Phys.* **140**, 224703 (2014).
- [35] M. N. Iliev, M. V. Abrashev, H. G. Lee, V. N. Popov, Y. Y. Sun, C. Thomsen, R. L. Meng, and C. W. Chu, Raman spectroscopy of orthorhombic perovskite like YMnO<sub>3</sub> and LaMnO<sub>3</sub>, *Phys. Rev. B* **57**, 2872 (1998).
- [36] N. Koshizuka and S. Ushioda, Inelastic-light-scattering study of magnon softening in ErFeO<sub>3</sub>, *Phys. Rev. B* **22**, 5394 (1980).
- [37] S. Venugopalan, M. Dutta, A. K. Ramdas, and J. P. Remeika, Magnetic and vibrational excitations in rare-earth orthoferrites: A Raman scattering study, *Phys. Rev. B* **31**, 1490 (1985).
- [38] F. Genet, S. Loidant, and G. Lucazeau, Vibrational Normal Modes of the D<sub>2h</sub><sup>16</sup> Phase of BaCeO<sub>3</sub>: a Critical Comparison of Force Fields, *J. Raman Spectrosc.* **28**, 255 (1997).
- [39] M. Balkanski, R. F. Wallis, and E. Haro, Anharmonic effects in light scattering due to optical phonons in silicon, *Phys. Rev. B* **28**, 1928 (1983).
- [40] A. Debernardi, S. Baroni, and E. Molinari, Anharmonic phonon lifetimes in semiconductors from density-functional perturbation theory, *Phys. Rev. Lett.* **75**, 1819 (1995).
- [41] J. Serrano, M. Cardona, T. Ritter, B. A. Weinstein, A. Rubio, and C. Lin, Pressure and temperature dependence of the Raman phonons in isotopic γ-CuI, *Phys. Rev. B* **66**, 245202 (2002).
- [42] A. Debernardi and M. Cardona, Dependence of phonon linewidths in semiconductors on temperature and isotopic composition, *Nuovo Cimento D* **20**, 923 (1998).
- [43] P. Y. Yu and M. Cardona, in *Fundamentals of Semiconductors: Physics and Materials Properties* (Springer, New York, 2010), pp. 408.
- [44] I. Charrier-Cougoulic, T. Pagnier, and G. Lucazeau, Raman Spectroscopy of Perovskite-Type BaCe<sub>x</sub>Zr<sub>1-x</sub>O<sub>3</sub> (0 ≤ x ≤ 1), *J. Solid State Chem.* **142**, 220 (1999).
- [45] L.-Y. Huang and W. R. L. Lambrecht, Lattice dynamics in perovskite halides CsSnX<sub>3</sub> with X= I, Br, Cl, *Phys. Rev. B* **90**, 195201 (2014).
- [46] L.-Y. Huang and W. R. L. Lambrecht, First-principles calculations of phonons and Raman spectra in monoclinic CsSnCl<sub>3</sub>, *Phys. Rev. B* **91**, 075206 (2015).
- [47] J. Tauc, Optical properties and electronic structure of amorphous Ge and Si, *Mater. Res. Bull.* **3**, 37 (1968).
- [48] B. Okai, K. Takahashi, M. Saeki, and J. Yoshimoto, Preparation and crystal structures of some complex sulphides at high pressures, *Mater. Res. Bull.* **23**, 1575 (1988).
- [49] R. Zallen and M. L. Slade, Influence of pressure and temperature on phonons in molecular chalcogenides: crystalline As<sub>4</sub>S<sub>4</sub> and S<sub>4</sub>N<sub>4</sub>, *Phys. Rev. B* **18**, 5775 (1978).